Monte Carlo Simulations of Polonium Drift from Radon Progeny in an Electrostatic Counter

Devon Seymour

Advised by Richard Gaitskell

Brown University, Dept. of Physics,

Providence RI 02912, USA

May 4, 2017

Physics Motivation

During the past two decades, a standard cosmological picture of the universe (the Lambda Cold Dark Matter or LCDM model) has emerged, which includes a detailed breakdown of the main constituents of the energy density of the universe. This theoretical framework is now on a firm empirical footing, given the remarkable agreement of a diverse set of astrophysical data. Recent results by Planck largely confirm the earlier Wilkinson Microwave Anisotropy Probe (WMAP) conclusions and confirm that the universe is spatially flat, with an acceleration in the rate of expansion and an energy budget comprising approximately 5% baryonic matter, 26% cold dark matter (CDM), and 69% dark energy[1].

Astrophysical measurements on multiple length scales show that dark matter is consistent with like a particle model and not a modification of gravity. Gravitational lensing of distant galaxies by foreground galactic clusters can provide a map of the total gravitational mass, showing that this mass far exceeds that of ordinary baryonic matter.

The LUX-ZEPLIN (LZ) experiment will attempt to establish the existence of a type of dark matter known as WIMPs (Weakly Interacting Massive Particles), which have been predicted by SUSY (supersymmetry). The detector design is

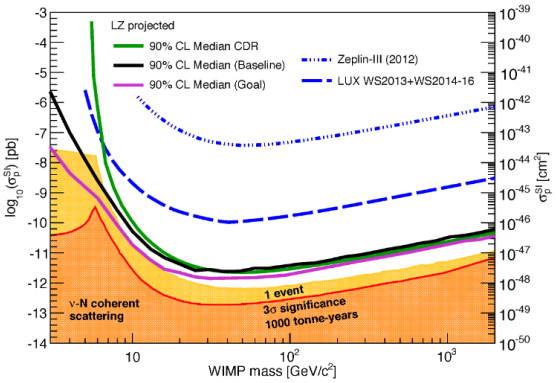

Figure 1: LZ sensitivity projections. The baseline LZ assumptions give the solid black curve. LUX and ZEPLIN results are shown in broken blue lines. If LZ achieves its design goals (e.g., reducing the radon background), the sensitivity would improve, resulting in the magenta sensitivity curve. The shaded regions show where background from cosmic neutrinos emerge.[1]

based on the use of liquid xenon as an interaction target for WIMP nuclear recoils. The desired detection sensitivity of the LZ detector is very low, much lower than the limit for LUX, the previous iteration of dark matter detector, as shown in Fig 1. The projected sensitivity of LZ is ∼50x better than LUX[1].

The detection rate for WIMP-Xe events is exceedingly low, ∼0.1 events/ton/day or lower, and WIMP events typically release little energy (∼1-100 keV), it is essential to have very high purity, and thus very low background in the detector. In order to help asses whether or not current background levels are acceptable, this Radon (Rn) counter was commissioned to assess whether or not the current level of Rn emanation of LZ materials is at an acceptable level.

It is critically important that the backgrounds in the LZ detector are reduced as low as possible due to the very small WIMP interaction rate. ^{222}Rn and ^{220}Rn easily diffuse though many materials due to their non-reactive properties as noble gases. The decay products produced in both radon decay chains can simulate WIMP-like events in the active volume of the detector under the right conditions and make the discrimination between backgrounds and signal more difficult, so it is particularly important to characterize the background in the LZ detector due to the emanation of these radon isotopes out of the detector materials.

^{222}Rn, which belongs to the ^{238}U decay chain, undergoes α-decay to a positively charged $^{218}Po^{+}$ ion in 65% of decays[3]. Using electric fields, these ions can be collected on the surface of a PIN diode. The second α-decay yields ^{214}Pb. The energy of this α-particle is measured using the PIN diode, assuming it is projected at an angle in the direction of the PIN diode, which will occur 50% of the time. After two subsequent β-decays, ^{214}Po is formed and undergoes α-decay after a combined half-life of 46.5 min. This α-decay will also be measured using the PIN diode under the same assumptions as the measurement of the α-decay from ^{218} Po. This counter

can also a detect another radon isotope, ^{220}Rn, which belongs to the ^{232}Th decay chain. ^{220}Rn undergoes α-decays to ^{216}Po^{+}. Following this decay, the ^{216}Po^{+} ion is subjected to the same collection method as listed above for ^{218}Po^{+} ions. Both radon decay chains are shown in Fig 2. Uranium and thorium affect background radiation levels, so detecting their radon progeny will help increase detector purity.

The detector needed for these radon measurements is a high-resolution solid-state detector. The original Case Western radon detector was constructed using a design similar to the detector used by the Super-K collaboration[4]. The Super-K detector utilized a silicon PIN diode, onto which the radon decay products were swept by a potential difference of several kV. A PIN diode uses an intrinsic, high-purity wafer of silicon, which is positively doped at the front entrance contact and negatively doped at the rear contact. For the purposes of this radon counter, the Ortec Ultra-AS was selected for its extremely low-background materials. In this case, the front contact is ion-implanted with boron and the rear contact is ion-implanted with phosphorous. The silicon wafer is reverse-biased (-50 V for the Ultra-AS) so that essentially no residual charge can flow between the positive and negative contacts, ensuring that any charge formed there due to charged particles will be measured accurately. When α-particles penetrate the entrance (positive) layer, millions of electron-holes are formed due to

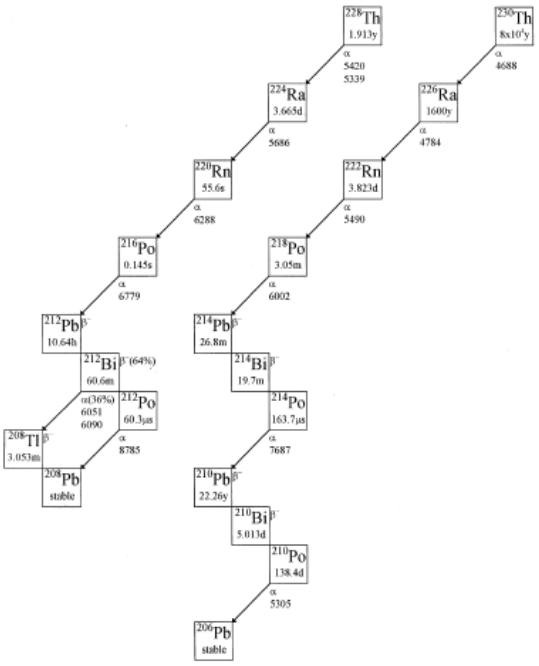

Figure 2: Uranium and Thorium decay chains. The half-lives, branching fractions, and decay energies (for α-particles) are shown.[5]

the semiconductor properties of the diode, and there is a pulse of current proportional to the energy of the incident particle. Thus, when α-particles penetrate the PIN diode, the current pulse can then be amplified, measured, and analyzed. At very low levels of radon, it is necessary to ensure that all signals are actually from radon. To do this, two criteria must be used. First, the incident α-particles must have the right energies (as shown in Fig 2); it will be possible to distinguish the α-particles and precisely measure their energy because of the high resolution (20 keV) of the PIN diode. Second, the α-decays must occur in time as dictated by their half-lives.

Radon emanation systems are required to meet sensitivity to ^{222}Rn at the level of 0.3 mBq from materials[1]. This is to minimize the background signal induced by fixed radioactivity in materials. Radioactivity associated with radon emanated into the instrument will contribute to the Electron Recoil (ER) and Nuclear Recoil (NR) counts, both of which are used for calibrating the system and detecting WIMP signals.

Counter Geometry/E-field Calculations

The primary vessel is a stainless steel nipple with one non-rotating flange and one rotating flange. At the top and bottom are reducing flanges to allow for attachment of a gas feed-through and a high-voltage feed-through, respectively. The gas feed-through is used to provide radon flow to the chamber from the emanation chamber, and the high-voltage feed-through is used to provide the bias voltage needed to operate the diode, as well as to generate the fields needed to collect polonium ion daughters. The PIN diode is mounted in the center using an aluminum cylinder. A Teflon seat is placed in between the aluminum and the diode to protect it from the high fields and to keep it electrically insulated from the grounded chamber. The interior schematic of the counter is shown in Fig 3.

COMSOL Multiphysics 4.3b was used to model the counter and simulate the electric field. A cross-section of the COMSOL model of the interior is shown in Fig 4. The electrostatic details for the aluminum pedestal, Teflon support, and operational conditions were provided by Dr. Timothy Edberg, (University of Maryland, College Park). As shown, the interior of the simulated model has been simplified. These simulations also include the top area allowing the gas feed-through plumbing and the interior of the pedestal.

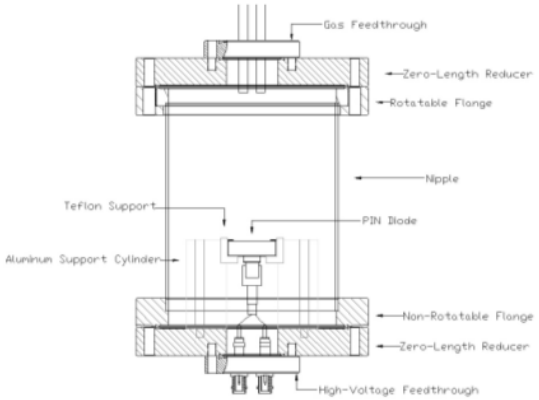

Figure 3: Case Western radon counter interior schematics[4]

As shown in Fig 4, for these simulations, there are three areas of importance for the electrostatic calculations: the volume above the pedestal (high E-field volume), the volume between the pedestal and counter wall (annulus volume), and the volume within the pedestal (dead volume). The importance of each area will be further explained. The volumes of each of these regions is displayed in Table 1.

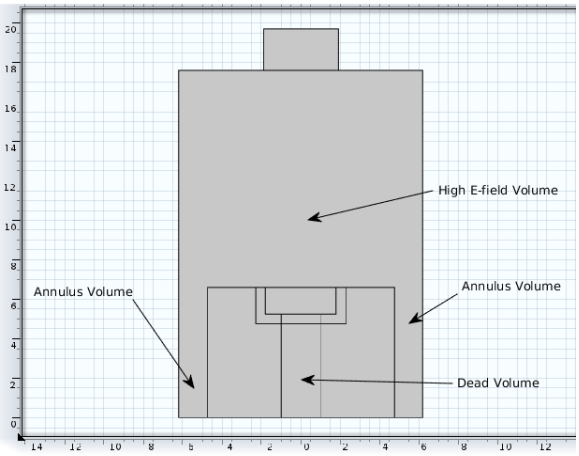

Figure 4: COMSOL model labeled with special regions of interest (dimensions in cm)

The dead volume of the counter is within the pedestal where the high-voltage cables enter the counter. Any radon decays that occur within this volume will not be detected, as these polonium ions cannot

reach the diode. This volume, as shown in Table 1, contributes ∼1% of the full volume of the counter and is negligible in comparison to the high E-field and annulus volumes.

The active volume consists of the high E-field volume, which contributes the majority of the volume of the counter, ∼80%, and the annulus volume, which contributes ∼20% of the total volume of the counter. Although this is much less than the volume of the high E-field region, special notice should be given to the annulus for this counter. Due to the counter's design, the magnitude of the E-field drops quickly towards the bottom of the annulus.

Full Volume (L)	1.698
Active Volume (L)	1.681
Dead Volume (L)	0.017
High E-field Volume (L)	1.352
Annulus Volume (L)	0.329

Table 1: Volume Breakdown for the Case Western ESC.

This effect is shown in Fig 5. While the upper region of the annulus is relatively viable for seeing particles, the deepest part of the annulus is "dead" volume, as the E-field is generally too weak to draw the particles towards the diode. Through particle drift simulations, it was seen that ∼40% of the annulus volume is viable for drawing particles towards the diode.

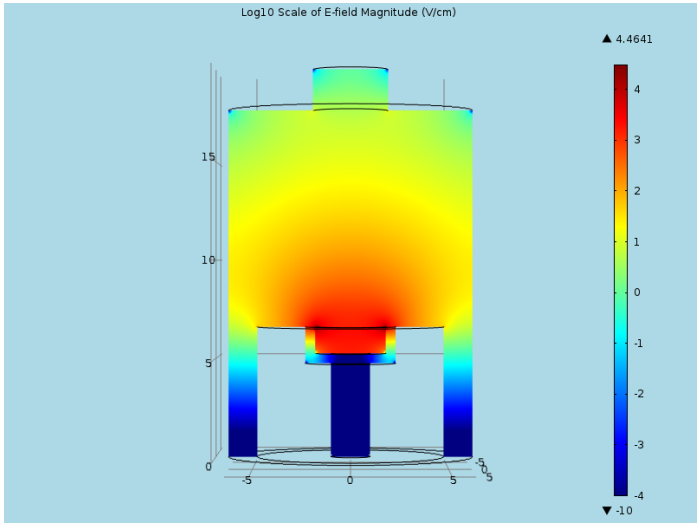

Figure 5: COMSOL Electrostatic Simulation at -2500 V (dimensions in cm). The colors represent the $\log_{10}$ of the magnitude of the E-field in $\frac{V}{cm}$.

Physics of the Drift

Since the focus of these simulations was ^{222}Rn, the description of the generation of particles and details of the drift will be explained using $^{218}Po^{+}$. In the ESC model, the position of a ^{222}Rn atom is chosen at random in Cartesian coordinates until the values lie within the ESC chamber. If the radon atom is successfully created within the ESC chamber, it is allowed to recoil in a random direction due to α-decay. If the ion's recoil length, which depends on the carrier gas pressure, does not take it into the wall of the ESC, then it is allowed to thermalize and start drifting towards the diode under the influence of the electric field. The derivation for the movement of the ions shown below comes from Eric Beauchamp Master's Thesis (Laurentian University, 2014)[3].

The drift of the Po^{+} ions in the counter is determined by the strength of the E-field and the mobility of the ion in the carrier gas. The mobility is given by the equation:

$$u = \frac{q}{k_B T} D \tag{1}$$

where q is the charge of the ion, k_B is Boltzmanns constant, T is the gas temperature, and D is the diffusion coefficient of the ion in gas. The diffusion coefficient depends on the diffusional mean free path, λ, and the root-mean-square speed of the atom, ν:

$$D = \frac{1}{2} \lambda \nu \tag{2}$$

The mean free path between the two species relates their collisional cross-section, σ, with the number density of the carrier gas, N.

$$\lambda = \frac{1}{N\sigma} \tag{3}$$

$$\sigma = \pi(r_{Po} + r_{gas})^2 \tag{4}$$

$$N = \frac{P}{k_B T} \tag{5}$$

The RMS speed of the gas ties together Boltzmanns constant, temperature of the gas, and the mass of the drifting ion, M_{Po}.

$$\nu = \sqrt{\frac{3k_B T}{M_{Po}}} \tag{6}$$

Putting these definitions together, one arrives at the following expression for the mobility, μ:

$$\mu = \frac{q}{2\sigma P}\sqrt{\frac{3k_B T}{M_{Po}}} \tag{7}$$

The drift velocity is the product of the mobility, μ, and the electric field, $\vec{E}$.

$$v = \mu\vec{E} \tag{8}$$

For each time-step in the simulation, the nearest grid point to the simulated ion's position is chosen to represent the local electric field before allowing the ion to drift to a new position. Time-steps are set to be 2.5 μs for the high E-field volume and the upper portion of the annulus volume, but 10 μs otherwise.

For these drift simulations, the following assumptions were made: The room temperature operating conditions, T, is assumed to be 293.15 K. The interior pressure gas pressure, P, is defined as the following expression:

$$P = Constant \cdot (1atm) \tag{9}$$

where Constant > 0. This condition is necessary to determine the optimal operating

pressure for this counter. Two carrier gases are used for these simulations, N_2 and He. Since the collisional cross-section σ depends on the radius of the carrier gas, the value of the mobility changes depending on the carrier gas used. The He radius is assumed to be the van der Waals radius, 140 pm, the Po^+ ion radius is assumed to be the van der Waals radius of the neutral ^{218}Po, 197 pm, and the N_2 radius is assumed to be twice the van der Waals radius of monatomic nitrogen, 310 pm.

It should be clearly stated that these simulations will be using both ^{218}Po and ^{216}Po. The three main differences between ^{218}Po and ^{216}Po should also be noted. First, ^{218}Po is slightly more massive than ^{216}Po, as evident by the atomic number. Second, the decay energy of ^{220}Rn $\rightarrow$ ^{216}Po is different from the decay energy of ^{222}Rn $\rightarrow$ ^{218}Po. This affects the recoil distance of the Po daughters. Lastly, the half-life for ^{218}Po is much longer than the half-life for ^{216}Po. The recoil and half-life differences are talked about later, as they are important factors in these simulations.

With these assumptions, it becomes possible to calculate the value of the mobility. The equation for the mobility gives a value of 1.79 $\frac{cm^2}{V \cdot s}$ for $^{218}Po^+$ ions and 1.80 $\frac{cm^2}{V \cdot s}$ for $^{216}Po^+$ ions in 1 atm of N_2 gas at 293.15 K. This value agrees well with the value of 1.88 $\frac{cm^2}{V \cdot s}$ in this calculation in Eric's paper [3]. Using this equation with 1 atm of He gas gives a value of 4.06 $\frac{cm^2}{V \cdot s}$ for $^{218}Po^+$ ions and 4.08 $\frac{cm^2}{V \cdot s}$ for $^{218}Po^+$ ions.

Loss Mechanisms

As shown in Fig 3, the simulation takes advantage of the cylindrical symmetry of the counter to reduce the model to a planar slice through its interior, simplifying the geometry and allowing the use of the axis-symmetric rz-plane. With this, Rn atoms are randomly generated until the coordinates lie within the counter chamber. Once the Rn population is successful, the simulation then determines if the particle

has been "lost," meaning that it will not be collected on the diode. This simulation considers four possible loss mechanism for generated particles: recoil, neutralization, in-flight decay, and diffusion.

Losses by Recoil

When ^{222}Rn atoms decay, the $^{218}Po^{+}$ ions are released with 100.48 $\pm$ 0.30 keV of recoil energy. The recoil of the progeny could send some ions into the ESC wall before they have a chance to thermalize and drift towards the diode. Using Lindhard and Scharffs model as a fairly accurate representation of stopping power in the 100 keV region, the stopping power decreases to approximately 20 $\frac{MeV \cdot cm^2}{g}$, which translates to a recoil range of 1 mm for $^{218}Po^{+}$ in 1 atm of N_2 gas[3]. The range increases for He gas due to its decrease in density. The model estimates a 1 mm recoil range at 1 atm for both carrier gases. This means that very few ions to be lost from recoiling into the ESC wall. The effect is marginal, although it is more noticeable at lower pressures.

As was previously stated, ^{220}Rn decay has a different energy than ^{222}Rn decay. These energies are shown in Fig 1. Because of these different recoil energies, the recoil lengths of $^{218}Po^{+}$ ions and $^{216}Po^{+}$ ions differ. For the simulation, however, the approximation is made that both particles recoil identically in both carrier gases. This simulation also uses a simple model to address the behavior of the recoil lengths of the ions at different pressures. Both particles use previously mentioned standard of 1 mm recoil length in 1 atm of pressure, while the recoil length is inversely proportional to the changes in pressure. In other words, a change in pressure to 2 atm leads to a 0.5 mm recoil length, while a particle in 0.25 atm will have a 4 mm recoil length. If the simulated particle has recoiled into a wall, the ion is recorded as "recoil," and the simulation continues with a new ion.

Losses by Neutralization

There is the chance of neutralization of Po^+ ions on its trajectory towards the diode, which would render it undetectable. This probability is determined by the carrier gas environment into which the the Po^+ has decayed. Po^+ ions can be neutralized by water vapor or NO_2 in nitrogen, as well as in air. The cause of this neutralization is attributed to trace gas molecules which scavenge electrons from the polonium recoil path and transfer the electrons to the ion. The presence of water vapor in the system would allow hydroxyl radicals to form from radiolysis and the following reaction would occur:

$$\begin{aligned} H_2O &\rightarrow H\cdot + \cdot OH \\ \cdot OH + e^+ &\rightarrow \cdot OH^- \\ \cdot OH^- + Po^+ &\rightarrow Po + \cdot OH \end{aligned} \tag{10}$$

It is assumed that the N_2 and He gas in the ESC is pure, however, there is still the chance of recombination of free e with $^{218}Po^+$ if the concentration of radon is high enough. Howard and Strange observed neutralization times upwards of 10 s for $^{218}Po^+$ for a range of radon concentrations, electric field strengths, and carrier argon and helium gas pressures[3]. If the lowest measured time of 10 s is taken as a worst-case scenario, this still gives ample time for $^{218}Po^+$ ions to drift to the diode.

For this reason, neutralization effects are not introduced for individual particles, but as an overall neutralization probability for each set of simulations. It was stated earlier that ^{222}Rn decays into a $^{218}Po^+$ ion in 88% of decays. This charge fraction is due to these neutralization effects. It is also assumed that ^{220}Rn behaves identically to ^{222}Rn for the simulation.

Losses by Diffusion

Following each time-step in the drift of the Po^+ ion, the ion is subjected to random movement, in accordance with diffusion theory. For three-dimensional diffusion, the particles new position is determined by:

$$MSD = \sqrt{6Dt} \tag{11}$$

where MSD is the mean squared displacement, D is the diffusion coefficient, and t is the time-step. MSD tells us how many Gaussian widths the particle will move away from its current position. To find this, a random number is chosen with normal distribution, using the particles position as the mean, and the MSD as the standard deviation. If the simulated particle has diffused into a wall before reaching the diode, the ion is recorded as either "wall," if the event occurs in the high E-field volume, or "annulus wall," if the event occurs in the annulus volume, and the simulation continues with a new ion.

Losses by In-Flight Decay

Each $^{218}Po^+$ ion produced has a half-life of $T_{1/2} = 3.1$ minutes, and each $^{216}Po^+$ ion produced has a half-life of $T_{1/2} = 0.145$ seconds. This is incorporated in the simulation by generating an exponentially-distributed random number based on the half-life for each ion produced. This predetermined lifetime is checked after each time-step in the simulation to verify that the ion has not yet decayed before reaching the diode. If the simulated particle has decayed before reaching the diode, the ion is recorded as "decay," and the simulation continues with a new ion.

COMSOL Simulations

As stated above, *COMSOL Multiphysics* 4.3b was used to simulate the interior geometry of the ESC as well as create the electric field maps used in the Monte Carlo simulations of the polonium drift. COMSOL allows the incorporation of very accurate details regarding the ESC, such as gas pressure and species, temperature, grounding and potential, and materials.

Shown here in Fig 6 is a two-dimensional slice of the full three-dimensional model used to simulate the ESC. When running these electrostatic simulations in COMSOL, the program first calculated the full E-field in the entire volume. After it finishes, the inherent cylindrical symmetry can be taken advantage of to reduce the three-dimensional result into the slice

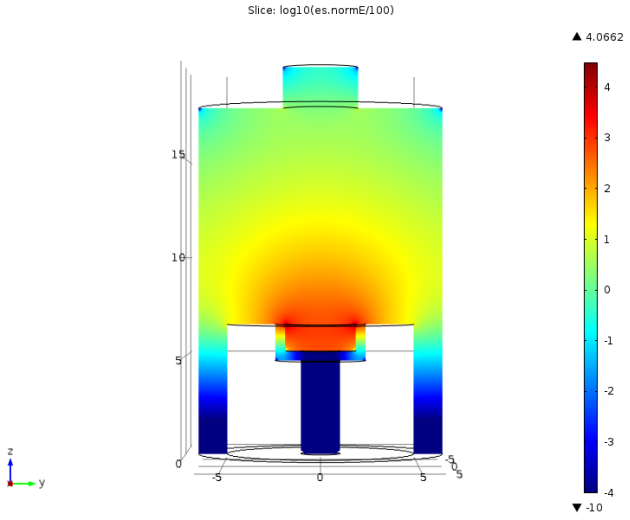

Figure 6: -1000 V E-field Slice (dimensions in cm). The colors represent the $\log_{10}$ of the magnitude of the E-field in $\frac{V}{cm}$.

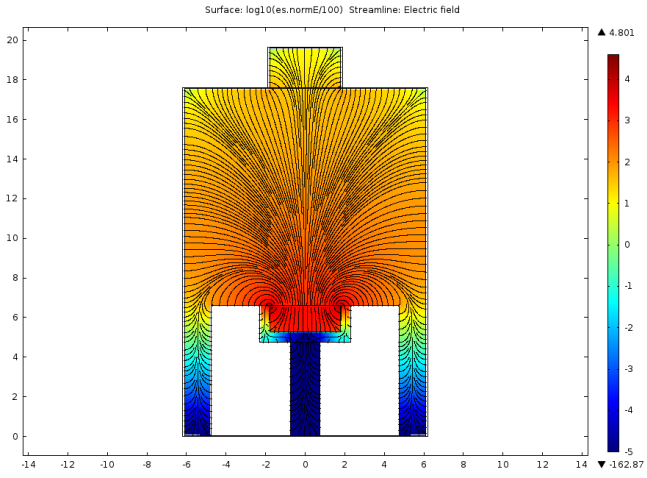

Figure 7: -3000 V E-Field with Streamlines (dimensions in cm). The colors represent the $\log_{10}$ of the magnitude of the E-field in $\frac{V}{cm}$.

shown. As such, there is no loss in using a slice instead of the full model as the basis for the Monte Carlo simulations, since the solution originated from the full model. Comparing Fig 5 to Fig 6, it is clear that at higher voltage, the E-field is stronger near the diode, and remains strong farther away from the source.

Shown in Fig 7 is a similar plot to both Figs 5 and 6, but at -3000 V and including the streamlines, or electric field lines, induced by the voltage on the diode. Due to the limitations of the program, the lines are not completely uniform in space, but it does manage to illustrate the electric field lines as a sanity check that the simulation is working properly. An important observation in Figs 5-7 is the strength of the E-field in the annulus volume of the detector. It was mentioned earlier that the annulus has a "dead" region, in which the E-field becomes too weak to effectively draw the ions into the diode. It should be noted that even at the strongest voltage possible for this detector, the annulus region still has the weakest E-fields and has a much lower probability of drawing an ion towards the diode. The extent of this weakening will be explored in the following section.

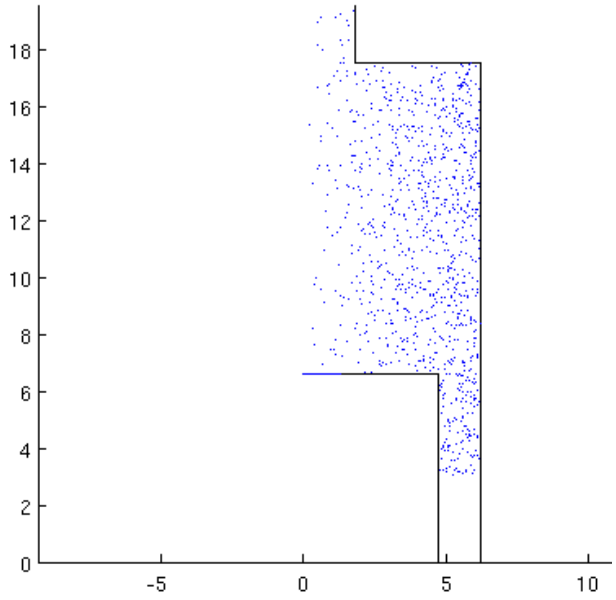

Figure 8: Sample Distribution (dimensions in cm)

MATLAB Simulations

Two notable aspects of Fig 8 are both the lack of simulated radon particles for r $<$ 0 and the lack of simulated radon particles in the lower region of the annulus. This is easily explained. Due to the symmetry of the two-dimensional slice, only one half of the interior was necessary for the Monte Carlo simulations. Particles are drift trajectories simulated on this right half (r $>$ 0) could be mirrored on the left half. This does have the caveat that, due to the random nature of the diffusion effects active during these simulations, the drift trajectories will not be exactly the same. However, for the high E-field region of the detector, the dominant source for movement of these particles is the E-field and not diffusion, such that the trajectories will remain relatively the same. The same cannot be said about the annulus volume, though.

The other noticeable aspect of Fig 8 is the partially simulated annulus region. As stated above, the viability for ion capture within the annulus falls rapidly. There are three simulation modes written into the code: using the entire active volume, denoted as full annulus, using only the high E-field volume, denoted as no annulus, and using part of the annulus deemed viable based on simulations (see Table 1 and Fig 4 for reference). These modes came about in an effort to maximize the detector's collection efficiency.

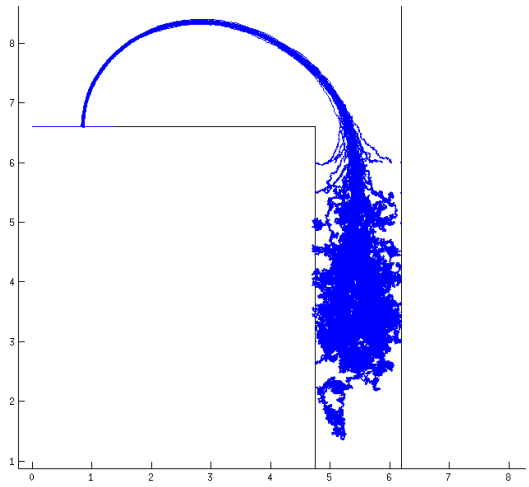

Figure 9: Annulus Test at -2500 V (dimensions in cm)

To determine where the viability of the annulus ended, probes of the annulus were

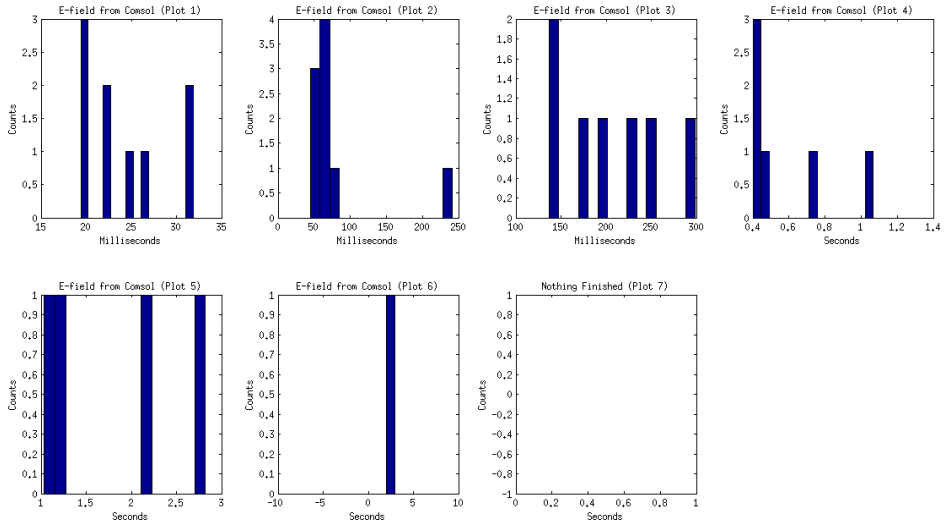

Figure 10: Arrival Time Histogram for Annulus Ring Depth Simulations.

performed. The entirety of this probe is illustrated in Fig 9. This was done using $^{218}Po^{+}$ ions by removing the effects of recoil and decay in flight, focusing solely on the interplay of the strength of the E-field and the strength of diffusion. The pressure of the N_2 carrier gas has also been lowered to 0.1 atm for this simulation, as well. Ten $^{218}Po^{+}$ ions were arranged equally spaced between the pedestal wall (to the left) and the detector wall (to the right) at set heights. This probe uses 3.0 cm, 3.5 cm, 4.0 cm, 4.5 cm, 5.0 cm, 5.5 cm, and 6.0 cm above the bottom of the detector. With the precise locations of these particles known, it is clear that as the depth into the annulus increases, the "messiness" of the trajectories also increases. The weakening of the E-field leaves diffusion as the primary source of movement.

Figure 10 shows the arrival time histograms for this set of simulations. The arrival times are increasing deeper into the annulus. The number of successful particles is decreasing deeper into the annulus. Both of these results are as expected. At a height of 3.0 cm above the bottom (Plot 7), none of the particles successful arrived at the diode for collection.

Figure 11 shows two such lines with more detail, with their starting heights listed. This settings for this simulation are slightly different from the the probe shown in Fig 9. The voltage has been changed to -1000 V, and the carrier gas is He. Through these simulations, it became evident that the two carrier gases show no significant difference. Near the top of the annulus, the ion collection is as viable as the high E-field region. However, the particles at 4.0 cm did not reach the diode successfully. There is this "hazy" region around 3.5 $\pm$ 0.5 cm where the E-field and diffusion strengths are roughly the same, so while the chances are low, there is a non-zero probability that particles deep in the annulus could reach the diode.

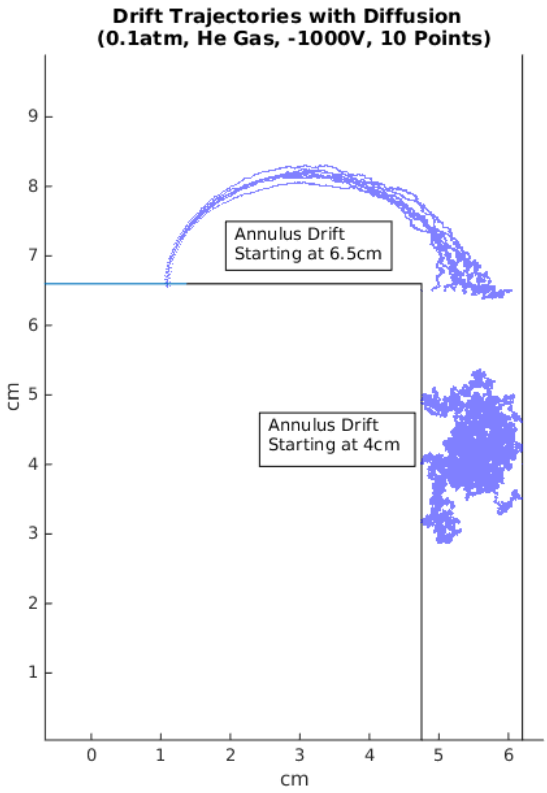

Figure 11: Annulus Drift Simulation (dimensions in cm)

^{216}Po^{+}

When the ESC is filled with clean He to allow for the ingrowth of the detector's background, the detector sees a ^{212}Po^{+} rate that is too high for the observed ^{216}Po^{+} rate. The hypothesis for the lower ^{216}Po^{+} rate is that the ^{216}Po^{+} ions are not being collected by the ESC, as they are decaying in flight before arriving on the diode. This suppresses the true ^{216}Po^{+} rate. We also assume that the ^{216}Po^{+} daughter, ^{212}Pb, is formed in as positively-charged ion. Thus, it would continue traveling towards the

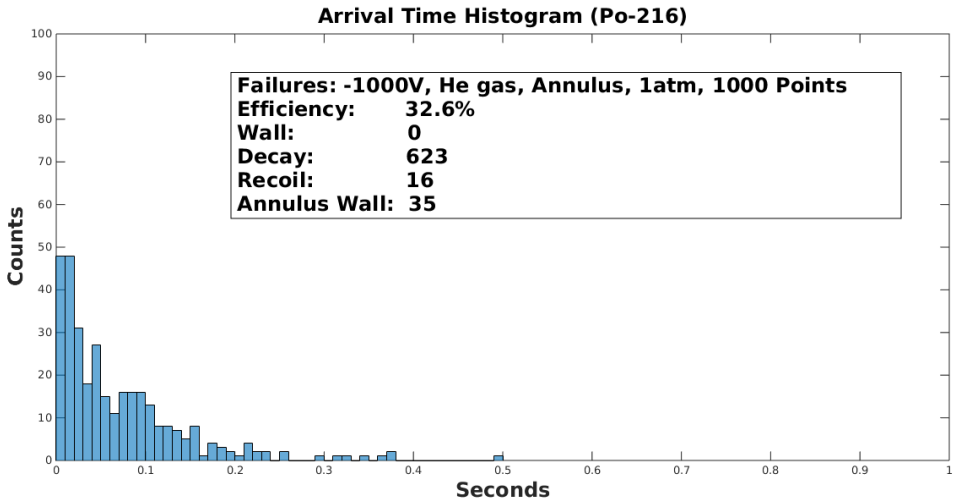

Figure 13: $^{216}Po^{+}$ Arrival Time Histogram

diode. This deposit of $^{212}Pb^{+}$ then beta decays (which goes unseen), but the ESC does see the alpha decays of the resulting $^{212}Bi^{+}$ and $^{212}Po^{+}$.

The simulation runs 1000 $^{216}Po^{+}$ ions in 1 atm of He gas, with -1000 V on the diode. These settings were chosen to most accurately match the actual electric field of the ESC and drift mechanics of the $^{216}Po^{+}$ ions for the in situ operating conditions. The simulation calculates 2.78 $\frac{cm^2}{V \cdot s}$ for value of the mobility.

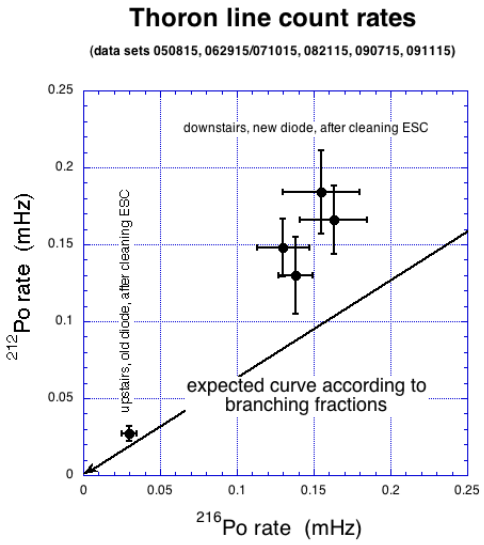

Figure 12: Actual vs Expected Thoron Count Rates

Figure 12 illustrates the results of this probe as the arrival time distribution and loss ratios for the $^{216}Po^{+}$ ions that completed the flight to surface of the diode. Only ∼33% of the simulated particles reached the diode with the given conditions. Figure 1 shows that the half-life of

^{216}Po is 150 ms. At -1000 V and 1 atm pressure, the vast majority of these ions decay in flight before reaching the diode, as shown in the table in Fig 12. This indicates that the drift time for $^{216}Po^{+}$ is long in comparison to its half-life.

The half-life for ^{212}Pb, however, is much greater than that of ^{216}Po, more than 10 hrs. Under our assumption that the ^{212}Pb forms positively-charged, it would not have the time constraint that $^{216}Po^{+}$ does. Thus, the $^{212}Pb^{+}$ arrives at the diode, and the subsequent ^{212}Bi and ^{212}Po alpha decays would take place on/near the diode. This would then show a higher $^{212}Po^{+}$ rate than $^{216}Po^{+}$, which is shown in Fig 13.

Results and Discussion

With all of the loss mechanisms included, a myriad of simulations were performed with combinations of voltages, pressures, and carrier gases to observe changes to various properties of the Po^{+} drift, such as the drift trajectories, arrival time histograms, and isochrone figures. Most importantly, these simulations were used to analyze changes in the counter collection efficiency.

Shown in Fig 14 is a sample of 100 randomly distributed $^{218}Po^{+}$ ions drifting towards the diode (blue line). This sample includes all loss mechanism due to drift (excluding neutralization) previously listed. The accompanying Fig 15 shows the arrival time histogram and a table of the collection efficiency and losses for these sample particles. For this sample, the counter had an 82% collection efficiency, which is primarily caused by the losses due to

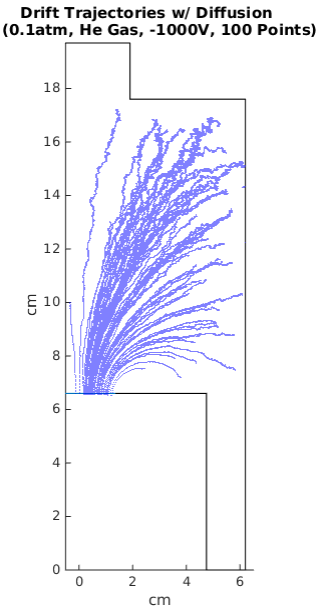

Figure 14: The tracks of a sample 100 $^{218}Po^{+}$ ions drifting towards the photo-diode.

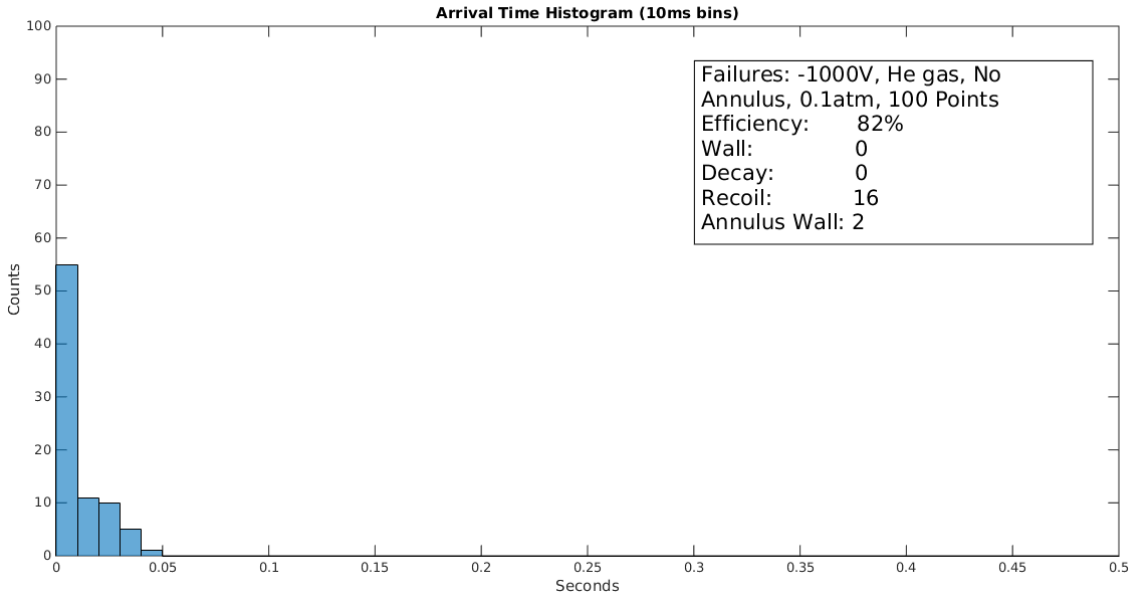

Figure 15: Arrival Times for Sample Simulation from Fig 14

the recoil from the Rn decay. As stated before, the recoil distance from decay is inversely proportional to the pressure.

For this sample, 0.1 atm was used as the operating pressure, leading to a recoil distance of 10 mm, or 1 cm. With a radius of 6.2 cm, particles can be lost to recoil in a significant portion of the counter volume. The mobility, μ, is also affected by changes in pressure, since:

$$\mu \propto \frac{1}{P} \tag{12}$$

Thus, smaller pressures lead to larger values of the mobility and drift velocity, which contributes to the small arrival times seen in Fig 15, with all successful particles arriving within 50 ms. From this sample, it is shown that changing the pressure increases losses from recoil while hastening the arrival time.

This leads to the isochrone simulation, useful for mapping the isochrones and seeing how the strength of the E-field varies with location. As shown in Fig 16, it works by populating the active region of the diode (straight green line) with 500

equally-spaced ions, reversing the components of the E-field, and removing diffusion and decay effects. Different step sizes were chosen when recording the isochrones. This was necessary to illustrate how the E-field changes in the corners of the counter. While it works well in mapping the high E-field region, it breaks down for the annulus region. This is still acceptable, since the isochrone simulation is most viable when diffusion effects are small in comparison to the drift distance, and Fig 9 shows that the diffusion effects are much larger in the in the annulus region. The isochrones also depend on the operating conditions used, as higher pressures would reduce the mobility, and therefore the drift velocity, while higher voltages would increase drift velocity. This would result in changing the spacing between the isochrones.

Of course, it must be mentioned that the isochrones simulation uses N_2 as the carrier gas instead of He, but assuming that the isochrone spacing between the two gases is similar, it is reasonable to say that if the starting locations of the drifting $^{218}Po^+$ ions in Fig 14 are compared to the isochrones in Fig 7, one can see why the arrival time histogram in Fig 15 makes sense.

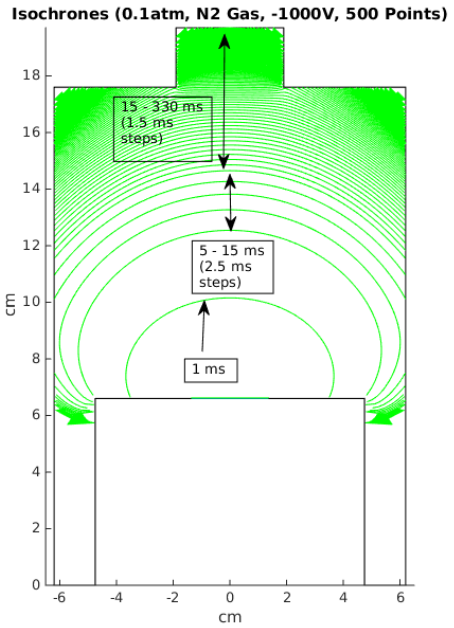

Figure 16: Isochrones

Figure 17 illustrates the collection efficiency of the Rn counter as a function of diode voltage for both $^{218}Po^+$ ions and $^{216}Po^+$ ions under the same operating conditions using 1000-point simulations for each data point. As shown, the collection efficiency for $^{218}Po^+$ ions plateaus quickly because it has a long half-life of 3.1 *minutes*. Therefore, the counter's ability to collect $^{218}Po^+$ is voltage-independent at ∼-500V. At this voltage, the efficiency for $^{216}Po^+$ is noticeably less. As the volt-

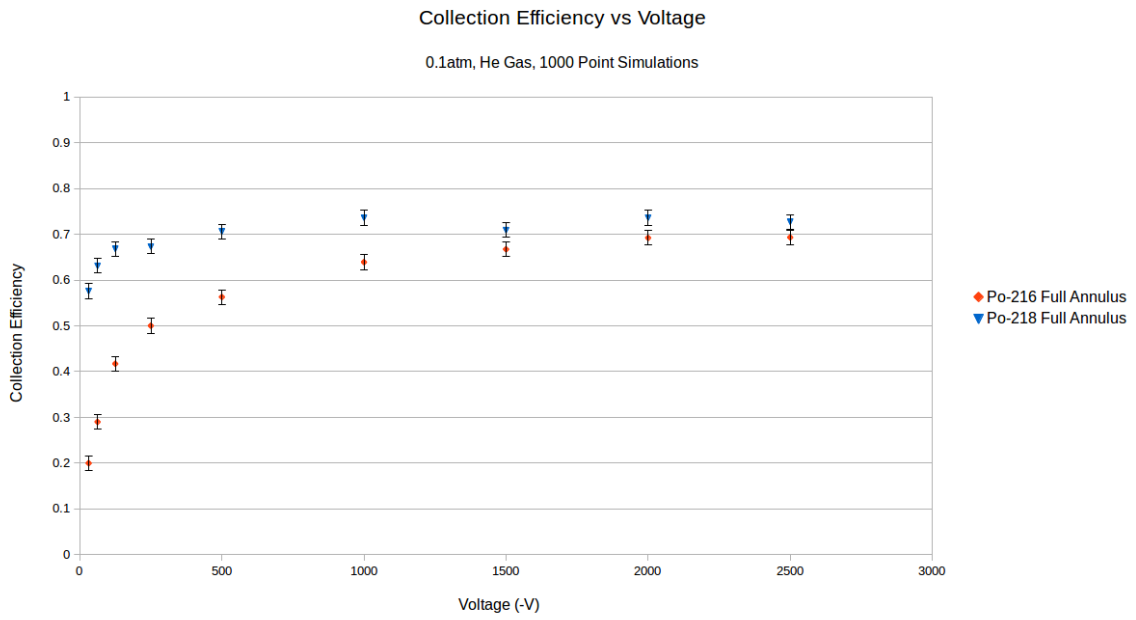

Figure 17: Voltage-Dependent Collection Efficiency

age increases, though, the collection efficiency for $^{216}Po^{+}$ ions begins to converge to the collection efficiency of $^{218}Po^{+}$ ions. This is because the effect of its 0.145 *second* half-life is being negated by the fast arrival times at higher voltages.

Figure 18 illustrates the collection efficiency of the counter as a function of gas pressure for both $^{218}Po^{+}$ ions and $^{216}Po^{+}$ ions under the same operating conditions using 1000-point simulations for each data point. For each ion, there are two simulations: "full annulus," which utilizes the full active volume of the counter, and "no annulus," which only includes the high E-field volume of the counter. The "no annulus" simulations were run in an attempt to improve the collection efficiencies by altering the interior geometry. Although removing the annulus volume is no longer an viable option, this data is still included as it also demonstrates the trends shown in the full annulus simulations.

At low pressures, both ions have the same general trend. As the pressure drops, the Rn decay recoil distance becomes larger, lowering the efficiency as more particles

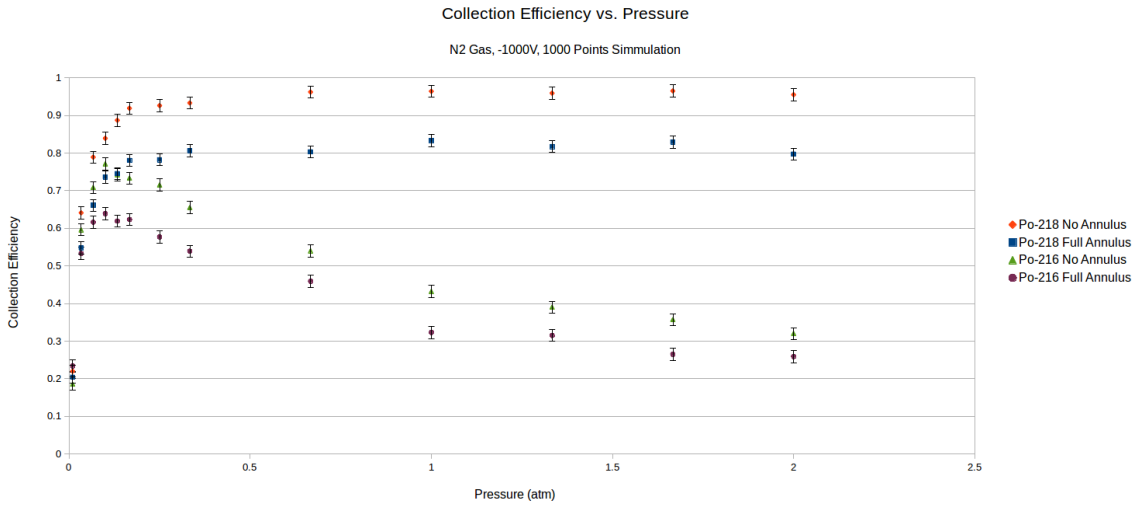

Figure 18: Pressure-Dependent Collection Efficiency

recoil into the wall. At the lowest pressure tested, 0.01 *atm*, the recoil distance becomes 100 *mm*, or 10 *cm*, comparable to the diameter of the counter, 12.4 *cm*. However, there is a very large divergence at higher pressures. As shown above, the counter's ability to collect $^{218}Po^{+}$ ions is pressure-independent above 0.25 *atm*, and unlike the plateauing collection efficiency for the $^{218}Po^{+}$ ions, the collection efficiency for $^{216}Po^{+}$ ions peaks at 0.1 *atm* under the listed operating conditions and drops as pressure increases.

This discrepancy is again rooted in the two vastly different half-lives. As the pressure increases, the mobility, μ, become smaller, decreasing the drift distance at each time-step. This, in turn, makes the ions drift for longer periods of time. As stated above, $^{218}Po^{+}$ has a much longer half-life than $^{216}Po^{+}$, 3.1 *minutes* vs 0.145 *seconds*. As such, the collection efficiency for $^{218}Po^{+}$ is un-fazed by changes in pressure, since the drift times at higher pressures are still short in comparison to the half-life. This in not the case, however, for $^{216}Po^{+}$, where the drift times quickly surpass the half-life and affect the collection efficiency.

Conclusion

The data in Fig 17 and Fig 18 are important indicators of what the counter's operating conditions should be in order to maximize the collection efficiencies for both ions. Since both carrier gases were relatively similar in performance, maximizing the efficiencies depends on the pressure/voltage combination. Collecting $^{218}Po^{+}$ ions is rather simple. Due to its long half-life, there is a wide range of operating conditions that work equally well. There are numerous combinations of pressure and voltage that would facilitate $^{218}Po^{+}$ ion collection. Collecting $^{216}Po^{+}$ ions, however, is slightly more challenging. Due to its half-life, there is a very narrow range of operating conditions at low pressure that maximize the collection efficiency. However, due to the low pressure, there is a constraint on the maximum usable voltage in order to prevent sparking. With these simulation, though, it is possible to optimize our operating conditions for each species of ion.

References

[1] Mount, B. J., eta al. "LUX-ZEPLIN (LZ) Technical Design Report." [1703.09144] LUX-ZEPLIN (LZ) Technical Design Report. 27 Mar. 2017. Web. 2 Apr. 2017.

[2] Verbus, J. "Low Background Radon Emanation Counting for the Large Underground Xenon Dark Matter Detector." 29 Apr. 2009.

[3] Beauchamp, E. "RADON REMOVAL FROM GASEOUS XENON FOR THE ENRICHED XENON OBSERVATORY." 2014. "https://zone.biblio.laurentian.ca/handle/10219/2148"

[4] Shaman, N. and Shutt, T. "Building a Radon Counter to Characterize Radon in the Case Liquid Xenon Detector." 13 Dec. 2006.

[5] Wang, J., Andersen, T., Simpson, J. "An electrostatic radon detector designed for water radioactivity measurements." Nuclear Instruments and Methods in Physics Research A 421 (1999) 601609. 7 Aug. 1998